The complexity of the relationship between spontaneous brain activity and glucose metabolism

Tommaso Volpi
University of Padova https://orcid.org/0000-0002-5451-6710
Erica Silvestri
University of Padova https://orcid.org/0000-0002-1853-0777
Marco Aiello
IRCSS SDN, Napoli
Maurizio Corbetta
Department of Neuroscience, University of Padova
Alessandra Bertoldo (alessandra.bertoldo@unipd.it)
Padova Neuroscience Center

Article

Keywords: spontaneous brain activity, glucose metabolism, rs-fMRI

Posted Date: August 4th, 2021

DOI: https://doi.org/10.21203/rs.3.rs-728300/v1

The complexity of the relationship between spontaneous brain activity and glucose metabolism

Tommaso Volpi[1,2]*, Erica Silvestri[1,3], Marco Aiello[4], Maurizio Corbetta[1,2], Alessandra Bertoldo[1,3]*

[1] Padova Neuroscience Center, Padova, Italy
[2] Department of Neuroscience, University of Padova, Padova, Italy
[3] Department of Information Engineering, University of Padova, Italy
[4] IRCCS SDN, Naples, Italy

Correspondence and request for materials should be addressed to T.V. (tommaso.volpi@phd.unipd.it) and A.B. (bertoldo@dei.unipd.it)

Abstract

Brain glucose metabolism as assessed by [^{18}F]FDG positron emission tomography (PET) is expected to be significantly related to resting-state functional MRI (rs-fMRI) activity and functional connectivity (FC), but the underlying coupling model is still incompletely understood. Employing simultaneous acquisitions, we related [^{18}F]FDG standard uptake value ratio (SUVR) to 50 features pertaining to rs-fMRI 1) signal, 2) hemodynamic response, 3) static and 4) time-varying FC, and 5) phase synchronization. To assess which rs-fMRI variables better describe SUVR across regions, we employed a hierarchical approach, identifying the model at population level, and then estimating it on individual data. Multilevel modelling explained around 40% of the SUVR variance, with signal-related features as the most relevant fMRI variables. When the model was used to characterize between-network variability of the SUVR-fMRI coupling, the ranking changed. We demonstrate that local activity and synchronization are the most important predictors of glucose metabolism, while large-scale FC properties gain importance within specific networks.

Introduction

Brain glucose consumption can be assessed *in vivo* by [^{18}F]fluorodeoxyglucose positron emission tomography ([^{18}F]FDG PET) acquisitions[1], usually through semi-quantitative proxies like the standard uptake value ratio (SUVR)[2]. As evidenced by [^{18}F]FDG studies, glucose metabolism displays significant regional variability. The reasons behind this heterogeneity in glucose expense, however, remain largely unexplained. Crucially, most of the remarkable metabolic budget of the brain, ~25% of energy in the face of only 2% of body weight, is spent during rest[3,4]. This 'dark energy' of the brain[5] with unclear functional meaning is expected to be mainly employed for maintaining resting potentials and subthreshold synaptic transmission[6], since most of the energy budget of a neuron is utilized at the level of the synapses, rather than in the neuron's body[7].

The regional differences in brain metabolism are thus likely to be explained by variability in spontaneous activity, which has been extensively explored with blood-oxygen-level-dependent (BOLD) resting-state functional magnetic resonance imaging (rs-fMRI)[8,9]. In addition to spontaneous activity, the functional relationships between activity patterns of different brain regions may relate to glucose consumption as well[10]. To this purpose, rs-fMRI can be used to derive the so-called "functional connectivity" (FC), i.e., the statistical relation between BOLD signal fluctuations in different brain regions; this approach has led to the identification of a functional architecture of resting-state networks (RSNs) that recapitulate clusters of regions activated for specific functions[11,12]. FC can be estimated in a static fashion (sFC), but also with time-varying approaches (tvFC), which interpret FC as non-stationary and changing across adjacent time windows[13]; notably, both might prove relevant to metabolic consumption.

Metrics derived from network science can then be used to characterize the topology of sFC and tvFC, with correlations between areas represented as 'edges' connecting 'nodes', and nodes described in terms of their centrality ('hubness'), number of connections, and so on[14,15].

While rs-fMRI studies have provided a wide range of information on the properties of spontaneous activity, the physiological underpinnings of these results remain poorly understood, as the BOLD signal arises from a complex combination of cerebral blood volume (CBV), blood flow (CBF) and metabolic rate of oxygen ($CMRO_2$)[17,18], and is indirectly and nonlinearly related to neuronal activity through the hemodynamic response function (HRF)[19]; importantly, it is also subjected to significant contamination from systemic modulations, both hemodynamic (heart rate variability, vasomotion etc.) and respiratory (e.g., respiratory volume variability)[20].

Building upon the previous considerations, the relationship between the information provided by rs-fMRI and [^{18}F]FDG PET across brain regions needs to be thoroughly investigated with two main aims.

First, to better understand the sources of regional metabolic variability. In particular, we might wonder: 1) how much is the 'dark energy' of the brain related to local activity probed by the BOLD signal? 2) how much is instead related to local synchronization of the BOLD signal, i.e., a possible measure of neural population excitatory-inhibitory balance? 3) does inter-regional static synchrony play a more relevant role than more dynamic, time-varying interactions?

Second, the biological basis of the BOLD signal needs to be further characterized, an effort that would help turn rs-fMRI into a more specific biomarker; [^{18}F]FDG PET, being tightly linked to neural activity[7], despite its typically low temporal resolution, can provide important insight.

Some evidence on this relationship has started to emerge from sequential and simultaneous [^{18}F]FDG PET/fMRI acquisitions[21]. In particular, the mean BOLD signal and the amplitude of its low frequency fluctuations (ALFF) have been found to be associated with [^{18}F]FDG SUVR across voxels[22], with stronger correlations in specific brain regions[23,24]. With regard to the coupling between FC and metabolism, moderate associations between SUVR and global FC metrics were detected[23,25], with stronger and more consistent correlations for the regional homogeneity (ReHo) of BOLD (up to Pearson's r = 0.8), which is an index of local synchronization[26,27]. The topology of FC was also found to be important, with more central nodes having a stronger relationship between their FC and metabolic consumption[23]. In addition, the relationship between SUVR and local and global FC has been described as a power law or exponential model, especially in some specific networks[25,28]. The variability in the [^{18}F]FDG-fMRI coupling across networks has been highlighted in multiple previous studies[23,24], with demarcation between visual and default mode regions on one side, and frontoparietal regions on the other[28]. When the [^{18}F]FDG-fMRI coupling is assessed across subjects, however, much lower correlations between SUVR and rs-fMRI variables are detected in many studies[23,26,27]. In summary, somewhat inconsistent results emerge from the literature, with bivariate spatial correlations between [^{18}F]FDG PET and a handful of BOLD-derived metrics (ALFF, ReHo, voxel-wise FC) ranging from 0 to 0.64 in explained variance (R^2), and substantial differences across brain regions and networks, as well as a low correlation across subjects even in simultaneous acquisitions[23,27]. Notably, no study has ever attempted a multivariate integration of a wider range of rs-fMRI features, as well as a multilevel prediction of SUVR both at the population level and at the subject/network level.

We set out to fill these gaps in knowledge with a fully data-driven approach using simultaneously acquired [^{18}F]FDG PET and rs-fMRI data from two separately published datasets of 26 subjects[23,31]. After preliminary assessment of 50 rs-fMRI-derived variables, pooled into 5 categories, i.e., 1) signal, 2) HRF, 3) sFC, 4) tvFC, and 5) phase coherence (PC)[29] (see **Table 1** for the list of the features, their acronyms and a brief description) we set out to address the following questions.

1. which is the strength of the bivariate association between these rs-fMRI features and SUVR across the whole brain? And then, since regions with high vs. low metabolic consumption are expected to have quite different structural and functional properties[1,3,4], does this coupling change according to the ranking of brain nodes based on SUVR?

2. is it possible to explain group level SUVR variance across regions by combining rs-fMRI features, for the first time, into a multiple regression model? Is the group of selected features more populated by local or large-scale brain network metrics, and does it account for between-subject variability (BSV)[30]? Finally, which of the previously identified rs-fMRI features are more important to explain SUVR when multilevel modelling is performed across RSNs, i.e., which is the between-network variability (BNV) of the SUVR-fMRI association?

Table 1 – Extracted rs-fMRI features and their categories

Fifty fMRI-derived variables, divided according to the pool to which they belong: 1) signal, 2) hemodynamic response function (HRF), 3) static functional connectivity (sFC), 4) time-varying functional connectivity (tvFC), 5) phase coherence (PC). See **Supplementary Methods** for full description of the features.

Pools	*rs-fMRI Variables*
Signal	**med-BOLD**: median of the BOLD time series
	MAD-BOLD: median absolute deviation (MAD) of the BOLD time series
	skew-BOLD: skewness of the BOLD time series
	ApEn-BOLD: approximate entropy (ApEn) of the BOLD time series
	rApEn-BOLD: range ApEn of the BOLD time series
	AR-BOLD: reflection coefficient of the first-order autoregressive AR(1) model fit to BOLD time series
	ALFF: amplitude of low frequency fluctuations (ALFF) of BOLD time series
	ReHo: regional homogeneity of BOLD time series
	MAD-ReHo: MAD of the time-varying ReHo (tvReHo)
	CV-ReHo: CV% of tvReHo
	peaks-BOLD: number of BOLD pseudo-events
HRF	**peak-HRF**: height of HRF peak
	hrf-DEG: degree (DEG) of HRF correlation matrix
	hrf-STR: strength (STR) of HRF correlation matrix
	hrf-CC: clustering coefficient (CC) of HRF correlation matrix
	hrf-BC: betweenness centrality (BC) of HRF correlation matrix
	hrf-EC: eigenvector centrality (EC) of HRF correlation matrix
	hrf-LE: local efficiency (LE) of HRF correlation matrix
	hrf-GE: global efficiency (GE) of HRF correlation matrix
sFC	**s-DEG**: DEG of sFC
	s-STR: STR of sFC
	s-CC: CC of sFC
	s-BC: BC of sFC
	s-EC: EC of sFC
	s-LE: LE of sFC
	s-GE: GE of sFC

tvFC	**mdiff-DEG**: temporal median of the absolute value of 1st order differentials (mdiff) of DEG time series
	mdiff-STR: mdiff of STR time series
	mdiff-CC: mdiff of CC time series
	mdiff-BC: diff of BC time series
	mdiff-EC: mdiff of EC time series
	mdiff-LE: mdiff of LE time series
	mdiff-GE: mdiff of GE time series
	CV-DEG: coefficient of variation (CV%) of DEG time series
	CV-STR: CV% of STR time series
	CV-CC: CV% of CC time series
	CV-BC: CV% of BC time series
	CV-EC: CV% of EC time series
	CV-LE: CV% of LE time series
	CV-GE: CV% of GE time series
	SampEn-DEG: sample entropy (SampEn) of DEG time series
	SampEn-STR: SampEn of STR time series
	SampEn-CC: SampEn of CC time series
	SampEn-BC: SampEn of BC time series
	SampEn-LE: SampEn of LE time series
	SampEn-GE: SampEn of GE time series
PC	**med-LEig**: median of the Leading Eigenvector (LEig)'s time series
	MAD-LEig: MAD of LEig time series
	CV-LEig: CV% of LEig time series
	mdiff-LEig: mdiff of LEig time series

Results

Feature extraction and preliminary evaluation of rs-fMRI variables

The flowchart describing the preprocessing and preliminary analysis of the [^{18}F]FDG PET and rs-fMRI data is shown in **Figure 1** (see the **Methods** section for details).

The [^{18}F]FDG PET variable of interest is the SUVR, which was extracted for every region of the Schaefer cortical atlas[32] (200 parcels, supplemented by 18 subcortical regions[33]) in each subject, and will be considered as the dependent variable in every modelling approach from here onward.

The 50 rs-fMRI variables, extracted at the single-subject level and *a priori* subdivided into 5 pools, are reported in **Table 1**: the signal pool (1) contains features related to the basic statistics of the BOLD time series (median, variance, skewness), its complexity, its low-frequency fluctuations (ALFF), local coherence (ReHo) and high-amplitude events (peaks-BOLD); in the HRF pool (2), then, we placed the amplitude of the HRF peak, calculated using a blind deconvolution method[34], and the HRF correlation structure across regions described by means of graph properties; the sFC pool (3) characterizes FC calculated across the entire fMRI scan with graph theory metrics; the tvFC pool (4) assesses graph metrics' temporal variability across sliding windows[13]; finally, the PC pool (5) characterizes FC as coherence of BOLD phase[29].

Figure 1 – Flowchart of rs-fMRI and [^{18}F]FDG PET processing, feature extraction and analysis. Both rs-fMRI time series and [^{18}F]FDG SUVR data were parceled using the Schaefer cortical atlas (200 ROIs) and 18 subcortical ROIs. The parcel-wise rs-fMRI data were used to extract fifty features representative of five pools, i.e., 1) signal, 2) HRF, 3) sFC, 4) tvFC, 5) PC. The PET-fMRI coupling was investigated using bivariate correlation and multivariable multilevel modelling across subjects and across fMRI-based RSNs.

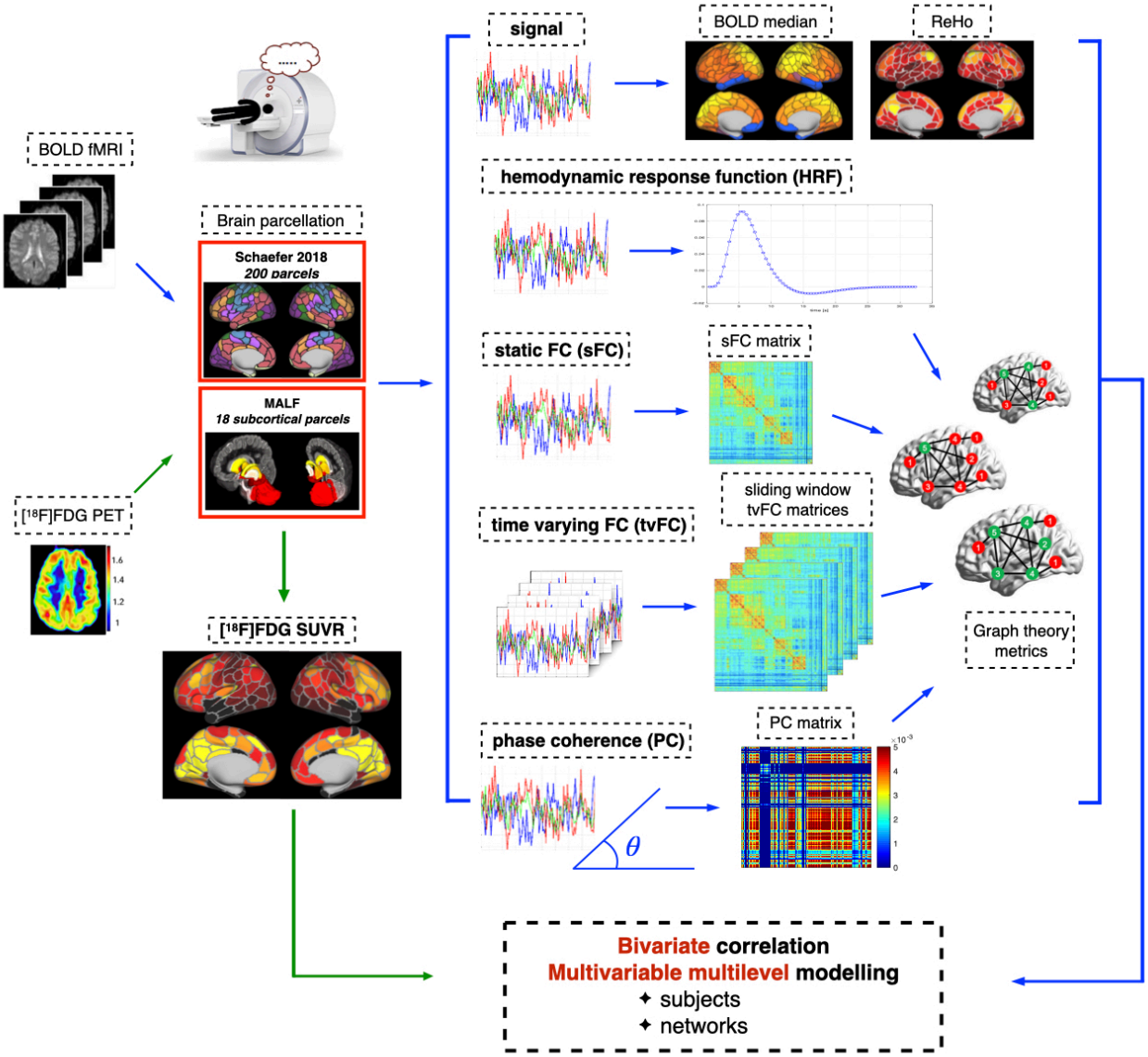

The Spearman's correlation matrix between the 50 rs-fMRI variables at group median level (i.e., by taking the parcel-wise median value of each feature across subjects) was computed (**Figure 2a**), in order to assess the relationships between the extracted features and their degree of redundancy: the clustering into 5 pools provided by *a priori* knowledge was fairly consistent with the observed correlation structure, with signal, HRF and sFC features (*upper block*) being clearly distinguished from tvFC features (*lower block*), which they are negatively correlated with, and PC variables demonstrating lower correlation with the rest. However, it was also noticeable that strong correlations between many variables were present, especially for the tvFC pool, and that a feature selection step was going to be necessary to use these variables in a numerically sound multivariable model of SUVR: the condition number $\kappa(X)$, which quantifies the level of correlation between predictors in a multiple regression context (i.e., their multicollinearity), was high ($\kappa(X) = 70.58$), way beyond the acceptability range[35], and this is known to result in unstable and unreliable models (see **Methods**).

SUVR vs. rs-fMRI: bivariate relationships

Before moving to the multiple regression framework, we began by investigating bivariate associations between SUVR and the extracted rs-fMRI variables at the group level, in the so-called naïve average data approach (NAD), as done by many previous studies[23,25,26]; here, however, a much wider range of fMRI-derived variables was explored. Many significant spatial associations between SUVR and rs-fMRI features were detected across the 218 analyzed regions, as assessed through Spearman's rank correlation ($p = 0.05$ significance level) with false discovery rate (FDR) multiple comparison correction[36]. The correlation coefficients are reported in **Figure 2b**.

Figure 2 – Bivariate correlations among rs-fMRI variables, and between rs-fMRI variables and SUVR. The pattern of Spearman's correlations (FDR-corrected, non-significant values shown in white) among rs-fMRI features, assessed at the group level and divided according to the pool to which they have been assigned (1) signal, 2) HRF, 3) sFC, 4) tvFC, 5) PC), is shown in (**a**). The rs-fMRI features are tested for association with group median SUVR across 218 brain regions (**b**) via Spearman's correlations (significant values after FDR correction are indicated with an asterisk).

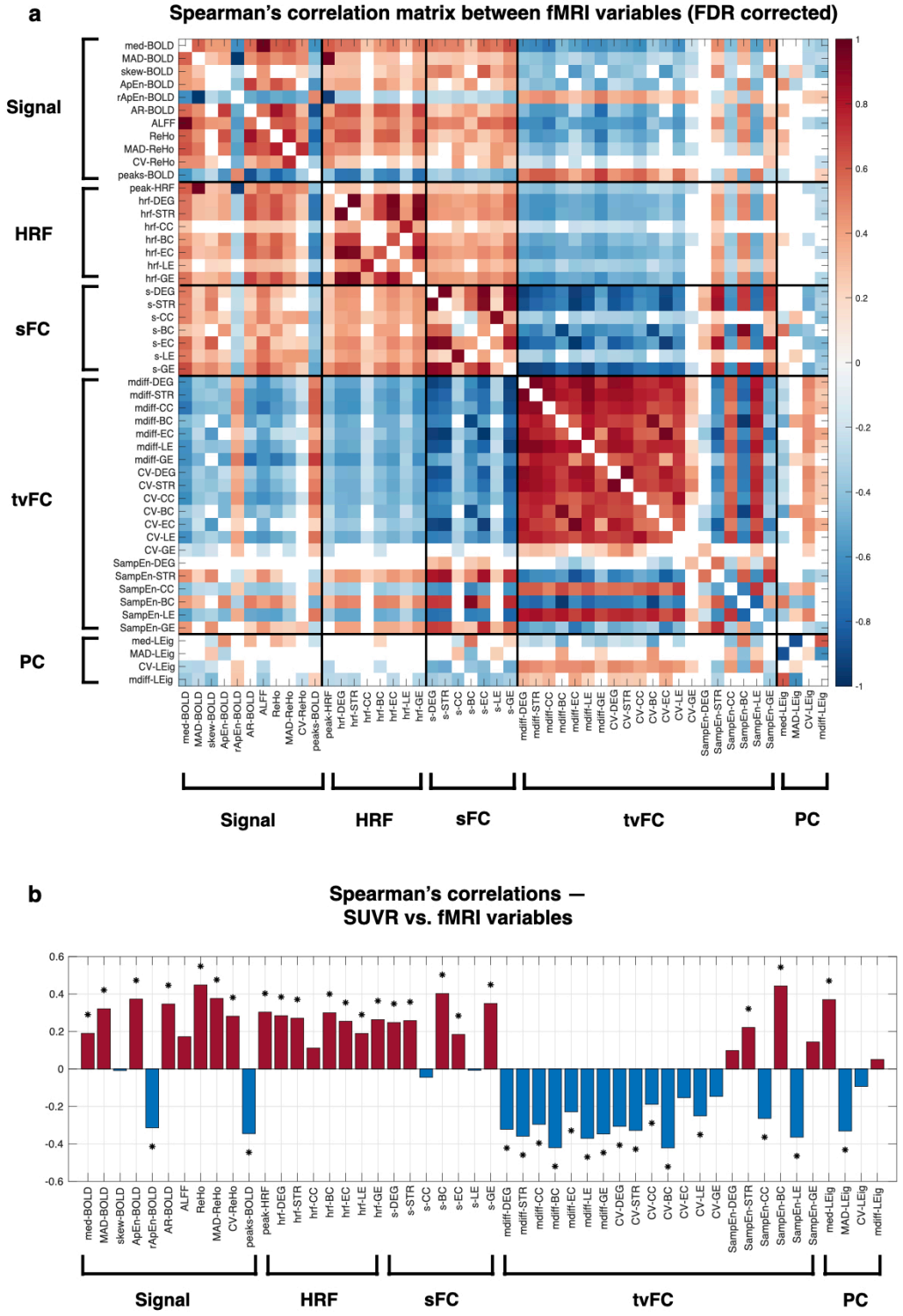

The strongest *positive* associations were with 1) ReHo (ρ = 0.45, p < 0.001), 2) s-BC (ρ = 0.4, p < 0.001), and 3) SampEn-BC (ρ = 0.44, p < 0.001), i.e., respectively 1) a measure of local synchronization of BOLD, 2) a sFC graph metric, betweenness centrality (BC), which describes a node in terms of its *global* connections in a graph, and 3) a measure of temporal complexity of the BC time series. The strongest *negative* correlations were mdiff-BC (ρ = -0.42, p < 0.001) and CV-BC (ρ = -0.42, p < 0.001) in the tvFC pool, both measures of temporal variability of BC.

In general, it can be noted that positive associations emerged for the majority of the signal-based, HRF and sFC-related features, while tvFC metrics displayed a consistent and never previously reported negative association with SUVR (**Figure 2b**). Notable exceptions amongst signal-based features are rApEn-BOLD (ρ = -0.31, p < 0.001), a measure of BOLD signal complexity, and peaks-BOLD (ρ = -0.34, p < 0.001), which quantifies the number of signal peaks exceeding one standard deviation from the baseline: both exhibited negative relationships with SUVR. Amongst tvFC features, SampEn-BC (ρ = 0.44, p < 0.001) shows a strong positive coupling with SUVR, in contrast to the behavior of the other tvFC metrics. Interestingly, the dynamics of local synchronization, i.e., MAD-ReHo and CV-ReHo, displays a positive association with SUVR as well.

Overall, it can be noted that the detected spatial correlations were at best moderate.

SUVR-fMRI associations are strengthened in low SUVR nodes

As the relationship between [^{18}F]FDG PET and rs-fMRI could be spatially heterogeneous, Spearman's correlations were also re-evaluated across groups of nodes selected according to linearly increasing percentiles of the SUVR distribution, i.e., by progressively retaining the highest SUVR values, from the 1st up to the 85th percentile, as well as linearly decreasing percentiles of the same distribution, i.e., by retaining the lowest SUVR values, from the 100th to the 15th (**Supplementary Figure S1**). The purpose of the analysis was to verify whether SUVR-fMRI associations would be strengthened in high SUVR nodes or, conversely, in low SUVR nodes, as SUVR provides a clear ranking of brain regions, that is expected to be related to crucial structural and functional properties, e.g., neuron-to-glia ratio, richness in neuroreceptors, excitatory-inhibitory activity[1,3,4].

Spearman's correlations (p = 0.05 significance level, FDR-corrected) between parcel-wise SUVR and all 50 rs-fMRI features (*rows*) are shown in **Figure 3a**, for each of the threshold levels along the SUVR distribution (*columns*). Going towards nodes with high SUVR (*right side of* **Figure 3a**) does not lead to any relevant effect for most features (except for three measures): therefore, hardly any strengthening of SUVR-fMRI relationships is detected in high SUVR nodes.

Interestingly, however, a marked increase in many of the bivariate associations can be observed by selecting nodes with low values of SUVR (*left side of* **Figure 3a**), with highly significant correlations even after FDR correction.

Figure 3 – The SUVR-*fMRI* correlation changes strongly in low SUVR nodes.

Spearman's correlations (FDR-corrected, non-significant values shown in white) between SUVR and all fifty rs-fMRI features (*y axis*) across nodes selected according to linearly increasing (*x axis - right*) and decreasing (*x axis - left*) percentiles of SUVR (**a**). The dashed black line shows the percentile with maximum correlation across features (i.e., nodes in the 1st - 40th percentile range). The histogram (**b**), on the right, highlights the chosen percentile in the SUVR distribution and the range of percentiles included in the correlation. The brain regions shown on the left, plotted on the cortical surface and subcortex, are the parcels over which correlations are assessed.

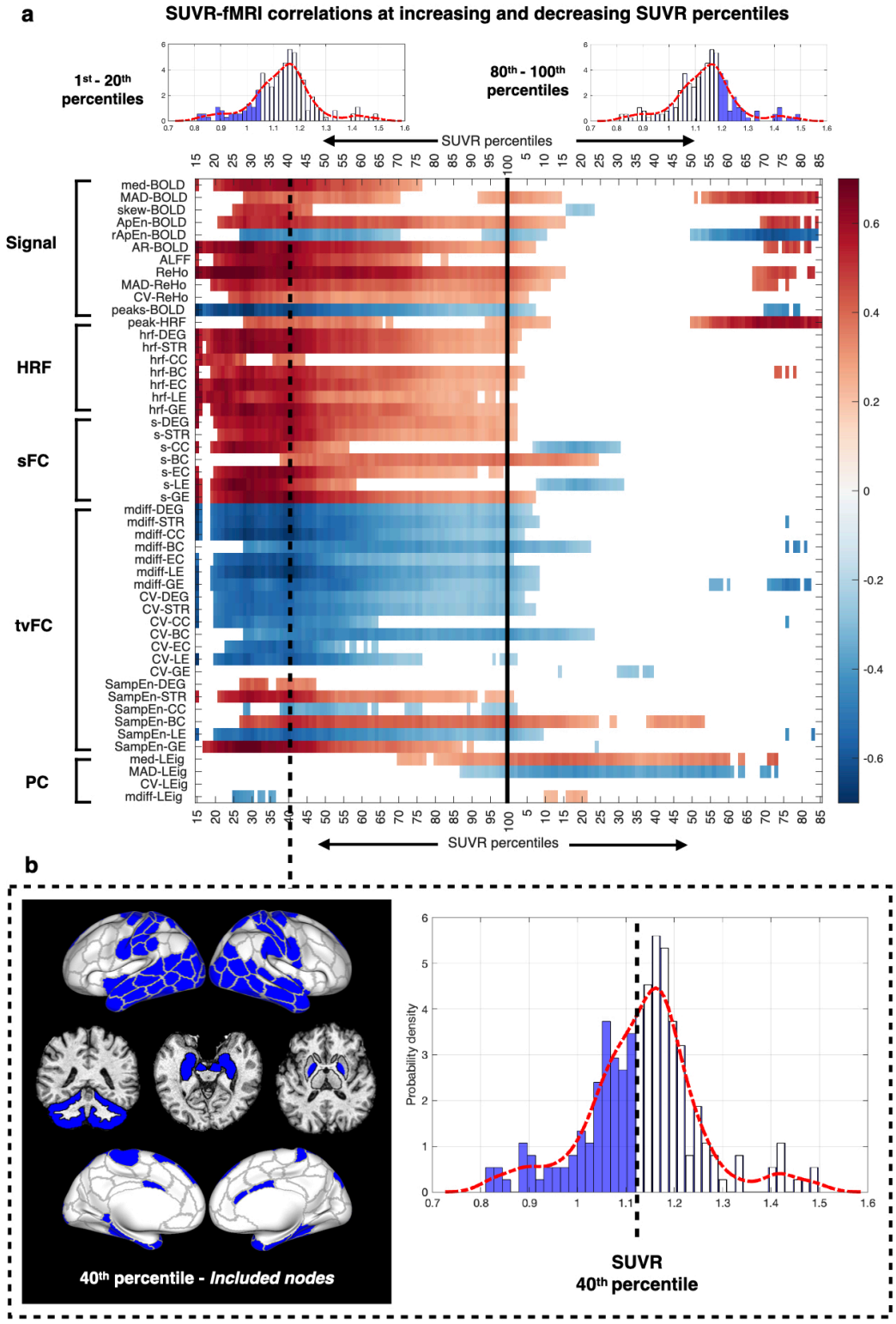

We then identified the percentile threshold corresponding to the highest total correlation value across features: the spatial pattern of the 87 nodes below the 40th percentile of the SUVR distribution is shown in **Figure 3b.** These parcels, where the SUVR-fMRI association is emphasized, mainly belong to temporal/limbic areas (including hippocampus), sensorimotor cortices, and subcortical regions, such as cerebellum and globus pallidus (**Supplementary Figure S1**).

This finding suggests the presence of *nonlinear* relationships between [^{18}F]FDG SUVR and most rs-fMRI features: tighter and more linear associations are present across a limited range of low SUVR nodes, with weaker coupling as SUVR gets higher. This nonlinear association was thus further characterized (see **Supplementary Results**), expanding on previous studies which were focused on specific networks and features[25,28].

SUVR vs. rs-fMRI: multivariable multilevel model

We then set out to assess which combination of rs-fMRI features was better able to explain SUVR across brain regions with multiple regression and multilevel modelling, in a fully data-driven way. In multilevel modelling, the model structure is usually known, or selected at the lower level, i.e., at the individual level[30]. However, as significant BSV in the SUVR-fMRI association is expected, especially for the rs-fMRI features, we chose to identify the model predictors at the population level (NAD approach), thus exploiting the denoising properties of averaging. The model structure selected at the group median level was then used for multilevel modelling across subjects to characterize the BSV of the SUVR-fMRI association, as shown in (**Figure 4**, *top*), trying to fully capitalize on the fact that [^{18}F]FDG and rs-fMRI data were acquired in the same subjects.

Maximum explanatory power of SUVR:

To assess the maximum explanatory power provided by the fMRI-derived features, we began by fitting an ordinary least squares (OLS) multiple regression model employing *all* the available features in a log-linear form (i.e., exploring the relationship between SUVR and the log-transformed rs-fMRI explanatory variables), to account for the detected nonlinearity (**Supplementary Results**): it can in fact be noted that the log-linear pairwise relationship between SUVR and each of the rs-fMRI features outperformed to the linear model in many occasions (62%). From now we will call this log-linear model.

The OLS model had an R^2 value of 0.62: the maximum explanatory power thus reaches up to around 60% of the SUVR variance, without fully saturating the variance despite marked overparameterization (i.e., 50 rs-fMRI predictors). Due to the high number of predictors and the presence of multicollinearity, the precision of numerous parameter estimates (expressed as coefficients of variation, CVs%)[37] was low, as expected (**Supplementary Figure S3c**).

Figure 4 – Multilevel modelling approach for subjects and networks. The multivariable model structure defined at the population level for the SUVR-fMRI relationship was used in a hierarchical model. The multilevel approach was first applied to individual data with subjects (*S*) as grouping variables (*S*, *top*), then with networks (*N*, *bottom*): fixed effects θ_S and θ_N describe the population parameters, and random effects η_{Si} and η_{Nj} describe how much each subject *i* or network *j* deviates from the population fixed effects for each of the selected parameters, i.e., the between-subject variability (BSV) and between-network variability (BNV) of the SUVR-fMRI model.

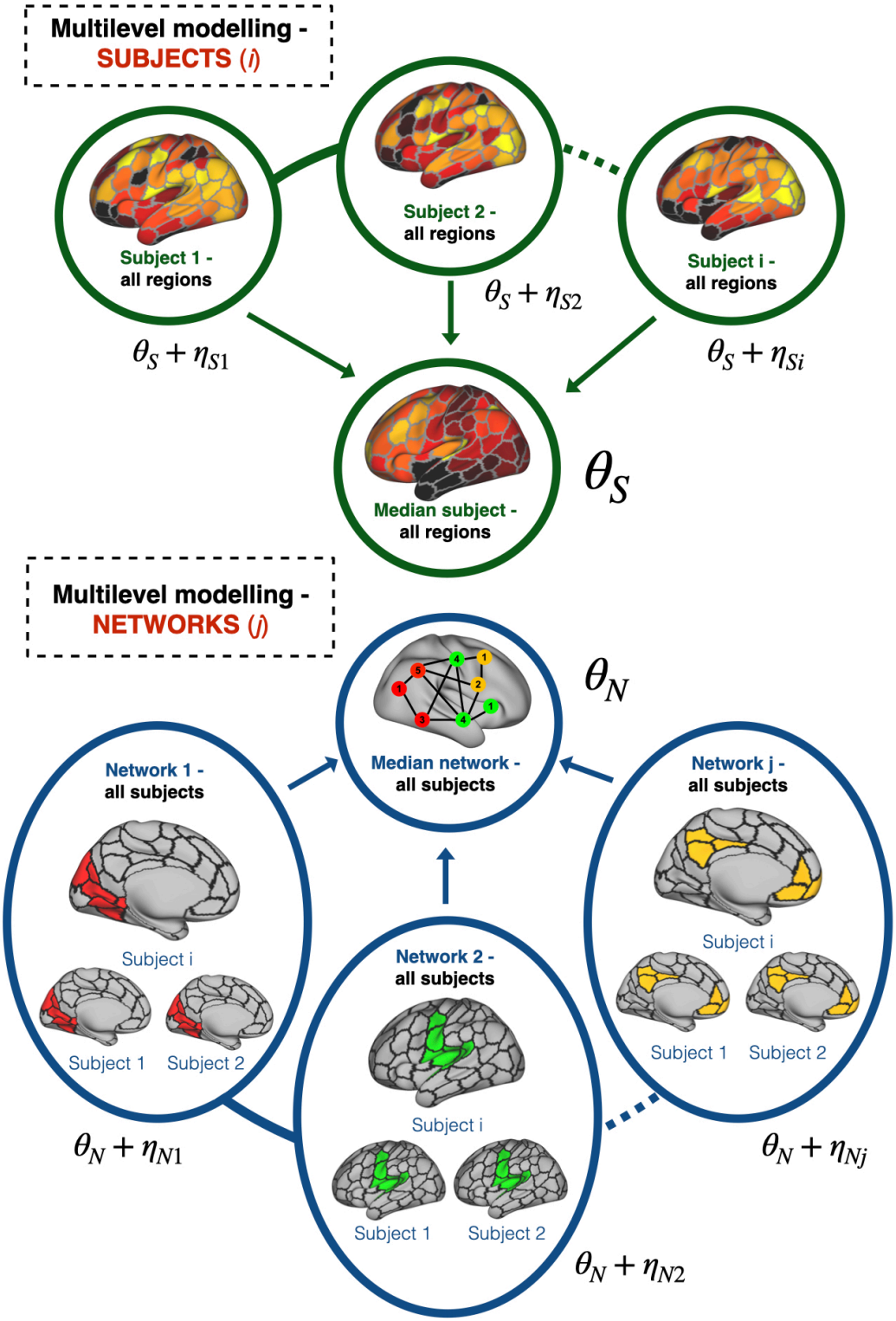

Assessment of a parsimonious and informative group level multivariable model:

Multiple feature selection approaches (eleven methods) were then explored. The results of each and the reason for the choice of the optimal approach are detailed in **Supplementary Results**.

The chosen feature selection process was performed in two stages. First, a sign-constrained non-negative least squares (NNLS) estimator[38] was employed; then, the NNLS estimates were refined with a second stage of feature selection with elastic net regression[39]. The reached solution was optimal in comparison with the other ten methods, in terms of both goodness of fit ($R^2 = 0.411$) and precision of the estimates (CVs% $\mu \pm \sigma = 66.73 \pm 17.79$ %). The selected rs-fMRI predictors are: 1) ApEn-BOLD, 2) rApEn-BOLD, 3) ReHo, 4) CV-ReHo, 5) peaks-BOLD, 6) hrf-LE, 7) s-BC, 8) CV-BC, 9) med-LEig.

The first five predictors belong to the signal and local synchronization pool, while the other four to the remaining groups of rs-fMRI features, suggesting only an *indirect* relationship with the large-scale network connectivity measures. Notably, most of the identified rs-fMRI predictors were chosen with high consistency across the employed feature selection methods, which highlights the robustness of their association with SUVR (**Supplementary Figure S4, Supplementary Figure S5**).

Multivariable multilevel model across subjects:

The hierarchical modelling framework was then applied to the individual data using the identified predictors, to characterize the BSV of the SUVR-fMRI association. The log-linear model identified at the group level was re-estimated using a linear mixed-effect (LME) approach[30]. The fixed-effect (θ_S) parameter estimates, which represent the equivalent of the parameters estimated at the group median level, are reported in (**Figure 5a**) with their standard errors (SEs). To get an accurate ranking of the most relevant predictors in explaining SUVR, the estimated θ_S were ordered by their relative contribution to the model using dominance analysis (DA)[40] (**Figure 5b)**. In terms of general dominance (see **Methods**), at the top was ReHo (48% of the total R^2), followed by peaks-BOLD (19%), CV-BC (11.74%), CV-BC (10.50%), s-BC (8.02%), ApEn-BOLD (3.67%), med-Leig (2.60%), hrf-LE (1.47%), rApEn-BOLD (0.02%). Notably, the features belonging to the signal pool collectively accounted for 76.17% of the hierarchical model R^2. The random effects (η_{Si}) describe the deviation from the group value of the parameters for a specific subject *i*, i.e., how much the parameters of each subject *i* are distant from the group-level estimates θ_S (**Supplementary Figure S7b**). In this case we found that the BSV in the SUVR-fMRI association is clearly non-negligible. In fact, the group-level θ_S estimates are very close to those obtained using the NAD approach, confirming the adequacy of the average approach in describing the relationship between the variables. However, as expected, the R^2 of the overall model, i.e., considering BSV, was lower and equal to 0.245, due to the capability of the multilevel mixed-effect approach to keep into account both

between- and within-subject variability. The R^2 values of the subject-level models are reported in **Supplementary Figure S7a**, and they display high variability (from 0.05 to 0.45).

The median across subjects of the model's residuals v_{Si}, which highlight how well the SUVR of each region is explained by the identified model, can be visualized in **Figure 5c**. Notably, high positive values are present in posteromedial cortex (posterior cingulate cortex (PCC) in particular) and subcortex (putamen): these areas identify nodes with high SUVR values which are not satisfactorily explained by the available rs-fMRI features. Importantly, this deficiency in explanatory power is highly consistent across subjects, as evidenced by the low variability (CVs%) of the residuals in those areas (**Figure 5d**).

Figure 5 – Multivariable multilevel modelling of SUVR across subjects. The multivariable log-linear model predictors chosen at the group NAD level are shown. Parameter estimates and standard errors for the fixed effects θ_S, which represent the parameters that best explain SUVR across regions at the group level (**a**). The relative importance weights produced by dominance analysis (DA), highlighting the proportion of the multivariable multilevel model R^2 explained by each predictor (general dominance) (**b**). Across-subject median (**c**) and CVs% (**d**) of weighted residuals v_{Si} of the multilevel model, plotted on the brain cortex and subcortex.

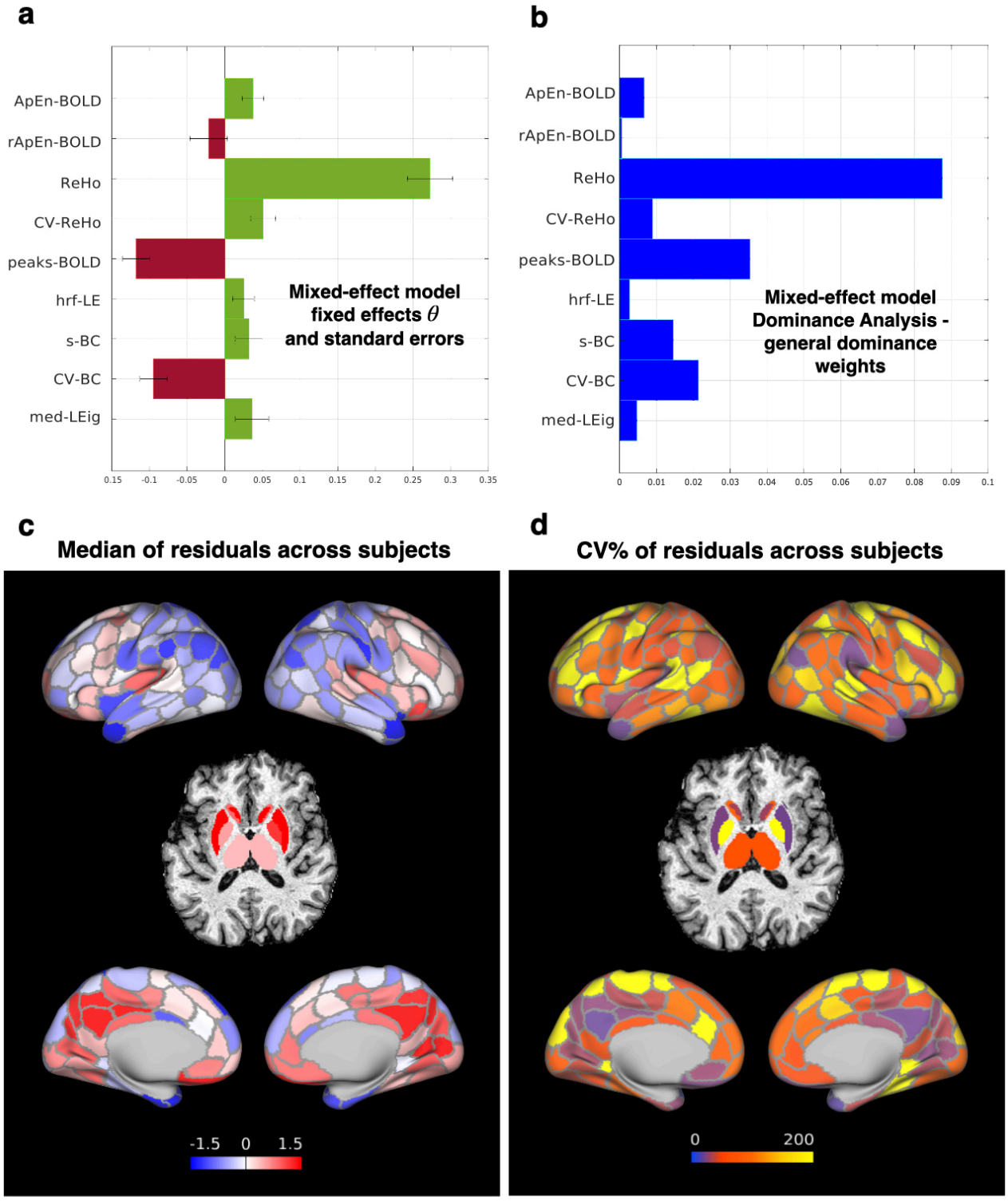

SUVR vs. rs-fMRI: multilevel model across networks

Finally, the log-linear model with the 9 selected rs-fMRI predictors was tested in its ability to describe the expected network-level variability of the SUVR-fMRI association (BNV), i.e., by considering only the parcels referring to specific brain networks. RSNs were here grouped according to the Schaefer' functional atlas in its 17-RSN partition[32], supplemented by 18 subcortical anatomical regions[33]. A multilevel modelling framework was again employed, but with RSNs as the grouping factor for individual level data, instead of subjects (**Figure 4***, bottom*).

The fixed effects θ_N and their SEs for the between-network model are reported in (**Figure 6a**). ReHo and peaks-BOLD are still highly relevant parameters in describing the SUVR across networks, together with ApEn-BOLD and CV-BC; rApEn-BOLD and hrf-LE, instead, lose importance, and their fixed effect θ_N becomes irrelevant (with a SE range crossing the zero-line). To confirm the ranking, DA was performed in this context as well: ReHo was still the most important predictor in terms of general dominance (explaining 23.24% of the model's R^2), followed by CV-BC (19.85%), peaks-BOLD (16.39%), s-BC (15.19%), ApEn-BOLD (11.46%), med-LEig (9.65%), CV-ReHo (2.55%), hrf-LE (1.80%), rApEn-BOLD (0.13%) (**Figure 6b**).

Notably, the R^2 of model prediction considering network-wise estimates is markedly lower than when subjects are used to cluster nodes. As shown in (**Figure 6c)**, the single RSNs are highly heterogeneous in terms of model R^2, ranging from around 0 to 0.32, with an overall prediction with $R^2 = 0.147$.

Figure 6 – Multilevel SUVR modelling across networks – parameter estimates and explained variance. The nine features chosen at the group level are shown. Parameter estimates and standard errors for the fixed effects θ_N, which represent the parameters that best explain SUVR across regions in an average network (**a**). Relative importance weights produced by dominance analysis (DA) in terms of the proportion of the between-network model R^2 explained by each predictor (general dominance) (**b**). Network-wise R^2 values, representing the percentage of SUVR variance explained by the mixed-effect model at the network level, plotted on the cortical surface and subcortex (**c**).

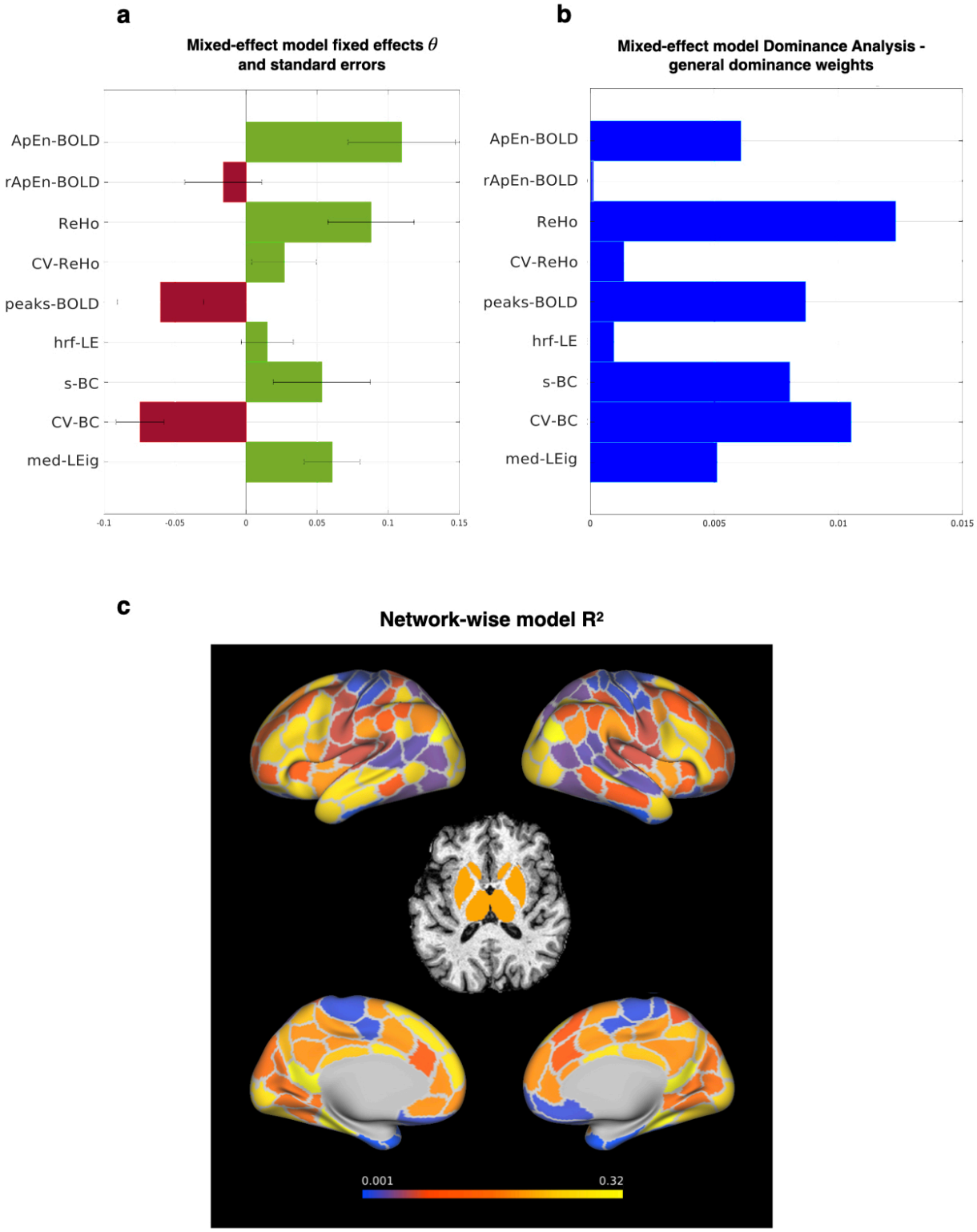

The BNV of the SUVR-fMRI association is measured by the random effects η_{Nj} for each network, with some RSNs displaying significant distance from the model estimates θ_N of the "average-network". To better assess this variability, the nine rs-fMRI predictors' parameter estimates ψ_{Nj} (i.e., sum of fixed effects θ_N and random effects η_{Nj} for every network j) were plotted (**Figure 7a**). We can observe that most predictors included in the multivariable model display heterogeneity across networks in their relationship with SUVR, with either positive or negative associations depending on the specific RSN, which cannot be captured by the average situation described by the fixed effects θ_N of (**Figure 6a**). Some predictors show notably consistent spatial patterns, and therefore, to assess their similarity, the correlation between their random effects was evaluated across networks (**Figure 7b**). Notably, although uncorrected for multiple comparisons, significant correlations ($p < 0.05$) can be found between the patterns of ReHo, CV-ReHo, hrf-LE and med-LEig, with strong positive weights for somatomotor network B (SM(B)) and also control network (CTR(C)). Another interesting pattern emerges for CV-BC, which displays both positive (CTR(A), VIS(B)) and negative weights (TEMP/PAR, LIMBIC(A), SAL/VAN(A), DMN(B)).

Finally, the network-wise ψ_{Nj} values were correlated across predictors, to assess how similar the RSNs were to one to another in terms of their SUVR-fMRI coupling (**Figure 7c**). When considering only significant correlations ($p < 0.05$, uncorrected), an interesting pattern emerges: some RSNs are fairly isolated from the rest of the brain in their SUVR-fMRI association pattern (e.g. DMN(A), DMN(C), VIS(A), VIS(B), SM(A), CTR(A)), with only 1-2 significant correlations with other RSNs; other RSNs, instead, have many significant correlations, and thus are similar to many other networks in their SUVR-fMRI coupling (SAL/VAN(A), DAN(A), DAN(B), CTR(B), CTR(C), DMN(B), LIMBIC(B), SUB).

Figure 7 – Multilevel SUVR modelling across networks – multivariable network-level estimates. Individual network parameter estimates (ψ_{Nj}, sum of fixed effects θ_N and random effects η_{Nj}, which describe the variability from the fixed effect for each RSN j), plotted on the brain surface for each predictor (**a**). Correlation matrix (non-significant values in white, p = 0.05, uncorrected) of the nine predictors' random effects η_{Nj} across RSNs (**b**). Correlation matrix (non-significant values in white, p = 0.05, uncorrected) of the RSNs' parameter estimates ($\psi_{Nj} = \theta_N + \eta_{Nj}$) across predictors (**c**).

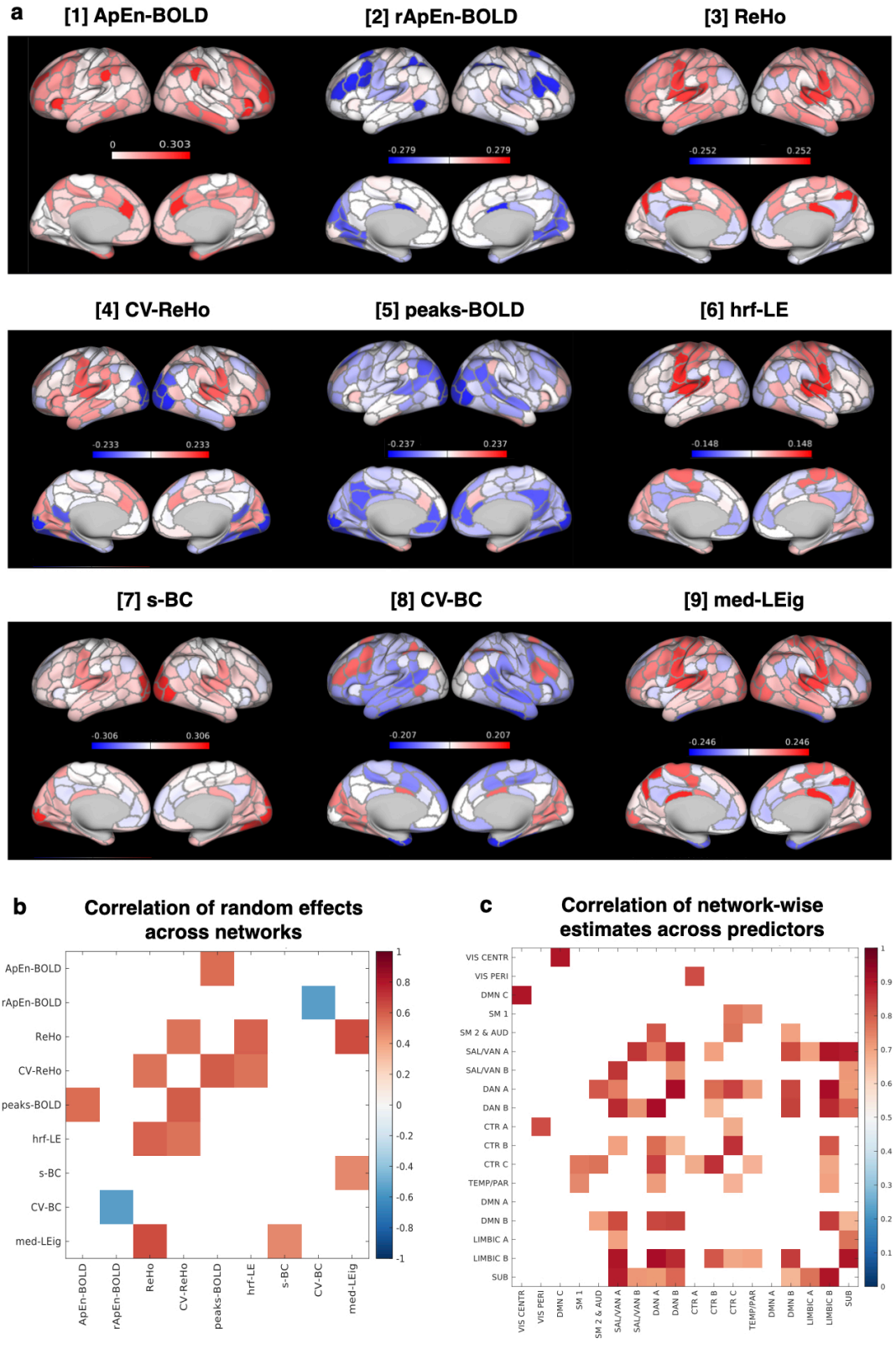

Discussion

In this work, we thoroughly investigated the spatial relationship between a wide range of features extracted from rs-fMRI and simultaneously acquired [^{18}F]FDG PET, while also accounting for the variability across subjects (i.e., BSV) and networks (i.e., BNV) in this relationship.

Relationship between SUVR and rs-fMRI through bivariate correlation

In addition to the rs-fMRI variables that have already been associated to SUVR, i.e., ALFF, ReHo, sFC strength[22,23,25], we extended our assessment to a wide variety of previously unexplored features, such as time-varying functional connectivity (tvFC) and HRF-related variables.

To our knowledge, the relationship between [^{18}F]FDG metabolism and FC temporal variability has never been tested before. While it is established that regions with stronger static FC tend to have higher cerebral blood flow[41] and higher energy metabolism[25], possibly reflecting the fact that they are also more strongly connected anatomically[42] (with recent work highlighting that structural connectivity graph properties are positively associated with [^{18}F]FDG SUVR[43,44]), the tvFC coupling with glucose metabolism is not established.

We found that tvFC (as captured by graph theory metrics' temporal variability) has a moderate-strong negative association with SUVR. The interpretation of this finding can be supported by knowing that sFC and tvFC graph metrics are negatively correlated, as clearly shown by the correlation matrix among rs-fMRI predictors (**Figure 2a**) and that the higher the strength of a static correlation across the entire rs-fMRI acquisition, the lower its temporal variability across time windows from the same acquisition[45]. However, examination of the relationships between tvFC and sFC graph metrics with SUVR suggests that a different pattern of correlations emerges, with tvFC-SUVR associations not being just the *inverse* of the sFC findings (**Figure 2b**). Similarly to our findings with [^{18}F]FDG, tvFC has been previously linked to L-[1-^{11}C]leucine PET, with regions having strong protein turnover displaying less temporal variability of their graph properties[46].

Interestingly, this negative association stands out when compared to CV-ReHo, which is instead positively associated with SUVR, implying that the dynamics of local synchronization vs. global FC may have different neurobiological underpinnings: this is in line with a rs-fMRI study which showed that, unlike with FC, static ReHo and time-varying ReHo are *positively* correlated[47].

Additionally, a strong negative relationship is found between SUVR and the number of BOLD pseudo-events (peaks-BOLD), which is related to the interpretation of the BOLD signal as a point process, with sparse neural events governing its dynamics[48]. While puzzling at first, one interpretation might come from considering that higher local oxygen consumption by active neurons is associated with decreased positive BOLD fluctuations[49], and therefore the higher the number of BOLD peaks and extreme events, the lower the oxidative metabolism and SUVR might be in that region.

We then examined how these relationships would be modulated by selecting parcels according to their ranking in the SUVR distribution. In order to better probe the spatial relationship between SUVR and rs-fMRI, which is heterogeneous across the brain[23,28], we chose to explore the changes in correlations selecting nodes from the SUVR standpoint, instead of according to FC properties[24,25]. Interestingly, nodes with progressively higher SUVR, which are expected to be the richest in terms of receptor density, local activity and inter-regional communications[1,3,4], did not show different relationships between metabolism and rs-fMRI, but the correlations with most rs-fMRI features became significantly stronger when considering nodes with progressively lower SUVR (**Figure 3**). This finding suggests that only in nodes with lower metabolism is the [^{18}F]FDG-fMRI relationship emphasized, implying the presence of a nonlinear association for most of the rs-fMRI features, not just for the previously explored metrics[25,28], with high SUVR nodes remaining unexplained by the available features. This nonlinear association was also assessed through model selection, with either an exponential, a power law or a log-linear relationship attributed to the majority (86%) of the evaluated bivariate associations (see **Supplementary Results**). The nonlinearity of the coupling between glucose consumption and BOLD is partly expected: 1) known nonlinearity exists in the associations between BOLD and neuronal activity[18], to which glucose metabolism is instead linearly related[7]; 2) nonlinear models such as power laws are common in biology, and in particular in metabolic budget[25]; 3) the [^{18}F]FDG coupling with local and global FC[25,28] has been previously described with a power law within specific areas; 4) nonlinear relationships between cerebral blood flow and glucose metabolism have been reported[50].

The multivariable multilevel model

To our knowledge, this is the first study to investigate the [^{18}F]FDG-fMRI coupling using a multivariable approach, attempting to identify the best subset of metrics, among a wide range of fMRI-derived variables, to explain SUVR variability across regions. Moreover, to fully capitalize on the fact that PET and fMRI data were acquired in the same subjects, we employed a multilevel modelling approach, with the selection of the best features performed at the group (higher) level, and modelling performed at the individual (lower) level, to characterize the between-subject variability of the SUVR-fMRI association (**Figure 4***, top*). The selected model consisted of nine rs-fMRI variables (**Figure 5 a, b**) which represented all pools of features: signal (ApEn-BOLD, rApEn-BOLD, peaks-BOLD, ReHo, CV-ReHo), HRF (hrf-LE), sFC (s-BC), tvFC (CV-BC), PC (med-Leig). The strongest predictors are related to the BOLD signal and its local synchronization properties (peaks-BOLD, ReHo), which consistently emerged as relevant across all feature selection methods (**Supplementary Results**). The fact that the SUVR-fMRI spatial coupling is emphasized when local

BOLD variables are involved might reflect the interplay between excitatory and inhibitory neural populations[51], which regulate CBF, a main ingredient in many fMRI-related features[17,18,52,53].

Overall, the explanatory power provided by BOLD rs-fMRI reached a 40% of the SUVR variance at the group level (24% across subjects). Zones of polarization in the model residuals emerged in subcortical (putamen), posteromedial (PCC), and lateral frontal regions, which could mainly be attributed to outliers with higher metabolism (**Figure 5c**), which are poorly explained by the available rs-fMRI features in a consistent manner across subjects (**Figure 5d**). These results point to the idea that the BOLD signal and FC, even though related to CBV, $CMRO_2$ and CBF[17,18], reflect the metabolic architecture established by [^{18}F]FDG SUVR only partially, even in simultaneously acquisitions, and that rs-fMRI FC and its graph metrics cannot be considered a proxy of glucose metabolism.

Moreover, the individual model R^2 values were variable across subjects, highlighting the fact that the SUVR-fMRI relationship displays significant between-subject variability, with subjects whose BOLD signal and FC architecture are more related to SUVR, and others that have hardly any relationship.

Next, we used the multilevel modelling approach and the identified predictors to characterize between-network variability, exploiting the fMRI-derived RSNs to group the individual data in a network-by-network fashion (**Figure 4***, bottom*).

Importantly, the rs-fMRI predictors selected for the between-subject model proved to still be relevant for evaluating the between-network SUVR-fMRI association, but their ranking, as assessed by dominance analysis, changed noticeably (**Figure 6b**), with static and dynamic FC features (CV-BC in particular) gaining importance in the model.

Moreover, when the network-wise effects are considered, significant positive and negative associations emerge for each of the nine predictors (**Figure 7a**). These patterns of predictors have some degree of similarity across networks, with a cluster of RSNs (subcortical, limbic, salience, dorsal attention etc.) being highly correlated, which implies they have a similar SUVR-fMRI multivariable association pattern (**Figure 7c**). Other networks, instead, seem to be more isolated in their SUVR-fMRI coupling (default mode, visual, somatomotor etc.), possibly reflecting their enrichment in high SUVR nodes (DMN, VIS) that are more difficult to explain using fMRI features (**Figure 5c**).

These findings add to and enrich previous work highlighting between-network variability in the SUVR-fMRI association through bivariate associations[23,28].

Notably, the regions where SUVR-fMRI *bivariate* correlations are higher (**Figure 3**) seem to fall into networks with fairly high R^2 values in the *multivariable* model (**Figure 6c**), confirming that the SUVR-fMRI coupling is emphasized in these regions. It is also important to underline that marked

regional heterogeneity has also been described in the coupling between [^{18}F]FDG SUVR and local CBF[54], which is likely to underlie some of the variability detected here due to CBF contributions to rs-fMRI variables.

Limitations

A comprehensive understanding of the relationship between [^{18}F]FDG PET and rs-fMRI will require simultaneous assessment of other features, such as CBF and $CMRO_2$, ideally probed by [^{15}O]H_2O PET[55] and [^{15}O]O_2 PET[56] respectively, which would thoroughly describe the effects of hemodynamics and oxidative and non-oxidative metabolism, possibly bridging the gap between these measures. Additionally, while the dataset employed here consists of standard rs-fMRI acquisitions (single-echo, TR of 2s, voxel size 3-4 mm, duration ~10 minutes), the BOLD-[^{18}F]FDG coupling would likely be improved by more advanced rs-fMRI methods (e.g. multi-echo imaging[57]), recordings of physiological variables (respiratory volume, end-tidal CO_2 and heart rate)[20], and regression of the CBF contribution[52] out of the BOLD signal and local coherence features.

For what concerns [^{18}F]FDG PET, it must also be remembered that SUVR, which was employed here as well as in all the literature on [^{18}F]FDG-fMRI coupling[22,23,25,27,28], may offer a biologically confounded view of glucose consumption: SUVR is in fact a semi-quantitative and relative index, which results from interactions between the rate constants of the [^{18}F]FDG compartmental model, i.e., K_1 (ml/cm^3/min), describing tracer uptake through the blood-brain barrier, k_2 (min^{-1}), describing its efflux into the venous blood, and k_3 (min^{-1}), quantifying the phosphorylation rate of the hexokinase in neurons and glia[1,2]. There is therefore the possibility that some of the contribution of CBF to the [^{18}F]FDG-fMRI coupling comes from SUVR, which is in fact highly correlated with the early, CBF-related frames of [^{11}C]PiB PET in healthy controls[59], as well as with PET-derived CBF estimates[54]. It is therefore likely that PET kinetic modelling will help disentangle the biological processes underlying both BOLD rs-fMRI and static PET estimates.

Conclusion

In conclusion, we thoroughly investigated for the first time the spatial relationship between [^{18}F]FDG SUVR and a wide range of features derived from rs-fMRI (pooled into 1) signal, 2) HRF, 3) sFC, 4) tvFC and 5) PC-based features) using simultaneous PET/fMRI data. Selection of low SUVR parcels led to a strengthening of SUVR-fMRI associations, implying the presence of a nonlinear relationship for many features. Moreover, a novel multivariable multilevel modelling framework was employed to identify the best subset of rs-fMRI predictors able to explain regional SUVR variance, highlighting that predictors based on the BOLD signal and its local synchronization (ReHo and BOLD pseudo-events, in particular) are the ones that are more tightly related to [^{18}F]FDG SUVR across brain

543 regions. This suggests a local contribution of CBF that should be tested for and, possibly, regressed
544 out from the BOLD signal.
545 Notably, the overall explanatory power provided by rs-fMRI on the regional metabolic variability did
546 not exceed 40% of the variance at the group level, with significant variability across subjects. When
547 multilevel modelling of the SUVR-fMRI coupling was carried out across networks, the selected
548 predictors were still relevant for description of RSN metabolism, but noticeable variability across
549 networks was present: new positive and negative associations emerged, and sFC and tvFC network
550 features gained importance. In conclusion, SUVR variability across parcels is only partly expression
551 of brain network organization described by rs-fMRI.
552
553

List of abbreviations:

ALFF, amplitude of low frequency fluctuations

ApEn, approximate entropy

BC, betweenness centrality

BNV, between-network variability

BOLD, blood oxygen level dependent

BSV, between-subject variability

CBF, cerebral blood flow

CBV, cerebral blood volume

$CMRO_2$, cerebral metabolic rate of oxygen

CTR, control network

CV, coefficient of variation

DAN, dorsal attention network

DMN, default mode network

FC, functional connectivity

FDG, fluorodeoxyglucose

FDR, false discovery rate

fMRI, functional magnetic resonance imaging

HRF, hemodynamic response function

LE, local efficiency

LIMBIC, limbic network

LME, linear mixed-effect

MAD, median absolute deviation

med-LEig, median of Leading Eigenvectors

OLS, ordinary least squares

NAD, naïve average data

NNLS, non-negative least squares

PC, phase coherence

PET, positron emission tomography

rApEn, range approximate entropy

ReHo, regional homogeneity

rs-fMRI, resting-state fMRI

RSN, resting-state network

SAL/VAN, salience/ventral attention network

SE, standard error

sFC, static FC

SM, somatomotor network

STR, strength

SUB, subcortical regions

SUVR, standard uptake value ratio

TEMP/PAR, temporo-parietal network

tvFC, time-varying FC

VIS, visual network

Methods

Data and Imaging protocols

The dataset includes 26 healthy subjects from two studies: 11 subjects (8 males; 52.2 ± 10.4 years), hereby referred to as dataset A (Munich)[23], and 15 subjects (6 males; 64.7 ± 7.9 years), i.e., dataset B (Naples)[31]. Subjects were scanned in *eyes open* condition while looking at a fixation cross. Exclusion criteria included a history of psychiatric or neurological disorders, use of psychoactive drugs or treatment with CNS-active medications, pregnancy, and MR-related contraindications. The subjects provided their informed written consent according to the Code of Ethics of the World Medical Association and the Institutional Review Board and Ethics Committee at the Technische Universität München, for dataset A, and the SDN Foundation, for dataset B. Both centers simultaneously collected [^{18}F]FDG PET and rs-fMRI data accompanied by a structural MR image on two identical Biograph mMR 3T scanners (Siemens Healthcare, Erlangen, Germany) equipped with the standard-supply head-neck coil (12-channel).

Dataset A: MRI data consisted in a structural magnetization prepared rapid acquisition gradient echo (MPRAGE) T1-weighted (T1w) image (TR/TE = 2300/2.98 ms, FA = 9°, 1 mm isotropic voxel size with 0.5 mm gap), 300 volumes of T2*-weighted gradient-echo echo-planar imaging (GE-EPI) with TR/TE = 2000/30 ms and voxel size of 3 mm isotropic (0.6 mm inter-slice gap). PET acquisition consisted in a saturated list mode (10 min duration), started 30 minutes post-injection and reconstructed with voxel size of 3.7 × 2.3 × 2.7 mm^3.

Dataset B: MRI data consisted in a similar T1- MPRAGE structural image and 240 volumes of GE-EPI for rs-fMRI with 4 mm isotropic voxel and TR/TE = 1920/32 ms. Simultaneous PET/fMRI measurements started 30 min post-injection, and PET images were acquired in sinogram mode for 15 min with reconstruction voxel size of 1.12 × 1.12 × 2.0 mm^3.

The interested reader should refer to the respective papers[23,31] for more detailed information on each dataset.

Data pre-processing

All subjects were identically pre-processed to obtain local metabolism information from [^{18}F]FDG PET data, and BOLD-based measures from rs-fMRI data, employing a pipeline similar to the Human Connectome Project (HCP) minimal preprocessing pipeline[60] with the addition of PET processing.

Structural imaging pre-processing

Structural T1w images were N4 bias field-corrected[61], skull-stripped, and segmented into grey matter (GM), white matter (WM) and cerebrospinal fluid. The brain cortex was delineated with Freesurfer (*recon-all* volume and surface reconstruction pipelines)[62], obtaining pial and GM-WM interface surfaces. Manual editing was performed to correct for surface delineation errors. Generated surfaces were resampled over the *fs_LR* mesh provided by *Conte69* atlas (symmetric-hemisphere mesh of 32k nodes) to obtain aligned cortical surfaces for each subject. The Schaefer functional atlas[32] was used to parcellate cortical surfaces into 200 parcels, grouped according to Yeo's 17 RSNs scheme[12] into Central Visual (VIS(A)), Peripheral Visual (VIS(B)), Somatomotor A (SM(A)), Somatomotor B (SM(B)), Temporal Parietal (TP), Dorsal Attention A (DAN(A)), Dorsal Attention B (DAN(B)), Salience/Ventral Attention A (VAN(A)), Salience/Ventral Attention B (VAN(B)), Control A (CTR(A)), Control B (CTR(B)), Control C (CTR(C)), Default Mode A (DMN(A)), Default Mode B (DMN(B)), Default Mode C (DMN(C)), Limbic A (L(A)) and Limbic B (L(B). The cortical regions were supplemented by 18 subcortical regions extracted from Freesurfer (bilaterally: Caudate, Putamen, Accumbens, Pallidum, Amygdala, Hippocampus, Thalamus, Ventral diencephalon, Cerebellar cortex) and delineated in single-subject space employing the Multi-Atlas Label Fusion (MALF) method[33]. Parcels corresponding to subcortical regions were assigned to the Subcortical (SUB) group.

PET data pre-processing

[^{18}F]FDG PET images, after normalization to injected dose and subject's body weight, were linearly resampled in T1w space with FSL's *flirt*[63] and intensity-normalized by the whole-brain average uptake[64]:

$$SUV = \frac{[^{18}\text{F}]\text{FDG concentration [MBq/ml]}}{\frac{\text{injected dose [MBq]}}{\text{body weight [kg]}}} \qquad SUVR = \frac{SUV_{\text{target}}}{SUV_{\text{reference}}}$$

SUVR maps were then parcellated in the same way as the rs-fMRI data, and parcel-wise SUVR was computed as the median value of the vertices inside a region. All pre-processing steps avoided any further spatial smoothing on both [^{18}F]FDG and rs-fMRI data.

Functional MRI data pre-processing

The first four rs-fMRI volumes were discarded to avoid non-equilibrium magnetization effects. The remaining volumes were corrected for slice timing difference by realigning them to the median volume, using FSL's *mcflirt*[63]. A template EPI volume was obtained with *antsBuildTemplate*[65] from realigned rs-fMRI data and used to estimate an affine transform (*flirt*, FSL), subsequently employed to map main tissue segmentations obtained from the pre-processed T1w image to the native EPI

space. Nuisance signals consisted in motion traces and their first order derivatives complemented by the first five temporal principal components, obtained after principal component analysis of WM and CSF EPI signals, explaining 70% and 50% of the average variance across subjects[66], which were regressed out from all brain voxels in native EPI space[67]. Regression residuals were finally resampled first to the T1w space and then on top of the mid-thickness cortical surface mesh with Connectome Workbench[68]. Finally, the BOLD signal was high-pass filtered with a cut-off of 0.008 Hz. No low-pass filter was applied, as the higher frequency components (0.1-0.25 Hz) of BOLD are likely to provide relevant neural information[69]. The vertex-wise BOLD signal was parcellated according to the Schaefer cortical atlas and the supplementary subcortical MALF parcels as previously described.

rs-fMRI feature extraction

Feature extraction as well as subsequent analyses were performed in MATLAB (ver. 2020a, The Mathworks, Natick, MA).

50 different features were extracted from the BOLD signal, either at the vertex or the parcel level. The extracted features were chosen as descriptors of different aspects of the BOLD 1) signal, 2) HRF, 3) sFC, 4) tvFC, and 5) PC. A list of the features and their acronyms is reported in **Table 1**. A detailed description of the features and how they were extracted can be found in the **Supplementary Methods**. The extracted features were then employed first in a bivariate correlation analysis against SUVR, and then in a multivariable multilevel modelling procedure to verify how much SUVR variance could be explained across the whole brain at the group level, as well as accounting for individual level information.

Bivariate analysis of the metabolism-fMRI relationship

rs-fMRI features vs. glucose metabolism across all brain regions

The bivariate relationship between node-wise SUVR and rs-fMRI properties was assessed at the group level (naïve average data approach, NAD), employing the region-wise median values across subjects for SUVR and each of the 50 extracted features. The association between fMRI-derived features and metabolism across nodes was separately tested via Spearman's rank bivariate correlation (significance level 0.05, corrected for multiple comparisons using the Benjamini-Hochberg FDR approach[36]).

rs-fMRI features vs. metabolism in specific clusters of nodes

The spatial heterogeneity in the [^{18}F]FDG PET-fMRI relationship, which has previously been reported[23,25], was probed by selecting clusters of nodes with increasingly high or increasingly low SUVR. The threshold level was determined by considering linearly increasing percentiles of the

SUVR distribution over all nodes, in the range going from the 1st to 85th percentiles, with step 1 (from 218 up to 33 nodes); moreover, in the opposite direction, nodes were selected according to linearly decreasing percentiles of SUVR, from the 100th to the 15th percentile (from 218 down to 33 nodes). Selected nodes at every level are reported in the binary matrix in **Supplementary Figure S1**. For each threshold level, Spearman's correlation between SUVR and all fMRI-derived features was calculated across the selected nodes, and FDR-corrected for multiple comparisons across thresholds and rs-fMRI features (significance level 0.05)[36]. The absolute values of Spearman's correlation were summed across the 50 fMRI variables for each percentile, to determine which threshold had the maximum correlation across features.

Multivariable modelling of the SUVR-fMRI relationship at the group level

The relationship between SUVR and each of the 50 rs-fMRI properties ($fMRI_{ip}$, for i = 1, …, 218 regions, and p = 1, …, 50) was then tested with four different bivariate models:

1) a linear model,

$$SUVR_i = \alpha_p + \beta_p \cdot fMRI_{ip}$$

2) a mono-exponential model,

$$SUVR_i = \alpha_p \cdot e^{\beta_p \cdot fMRI_{ip}}$$

3) a power law model,

$$SUVR_i = \alpha_p \cdot fMRI_{ip}^{\beta_p}$$

4) a log-linear model,

$$SUVR_i = \alpha_p + \beta_p \cdot \log fMRI_{ip}$$

which were compared in terms of their residual sum of squares (RSS). This bivariate model selection process led to choose the log-linear model for multiple regression modelling (see **Supplementary Results**).

At the NAD level, a multiple linear regression approach was employed to verify how much of the group-wise SUVR variance could be explained by the linear combination of different fMRI-based features. The ordinary least squares (OLS) problem was formulated as follows:

$$y = X\beta + \varepsilon$$

where y and ε are $n \times 1$ vectors of the response/dependent variable (i.e., SUVR) and the model error, and $X \in \mathbb{R}^{n \times p}$ is the matrix of p regressors (i.e., log-transformed rs-fMRI predictors), or design matrix. Before performing OLS regression, all predictors were z-scored, i.e., centered and scaled by their standard deviation (SD). The outcome variable, i.e., SUVR, was z-scored as well, so no model intercept needed to be estimated. The solution to the OLS problem was obtained as

$$\hat{\beta} = (X^T X)^{-1} X^T y$$

The model design matrix consisted of 50 parameters. The model was formulated as follows:

$$SUVR_i = \beta_1 \cdot \log fMRI_{i1} + \beta_2 \cdot \log fMRI_{i2} + \cdots + \beta_p \cdot \log fMRI_{ip} + \varepsilon_i$$

for each observation $i = 1, \ldots, n$. The relationships amongst the predictors were evaluated by Spearman's correlation (**Figure 2**), to assess the presence of strong correlations (i.e., multicollinearity). Since high multicollinearity amongst predictors is known to result in lower precision, switched signs of the coefficients, and a lack of statistical significance of the multivariable model[35], the ill-conditioning of the design matrix was quantified using the condition number, i.e.,

$$\kappa(X) = \frac{\sigma_{\max}(X)}{\sigma_{\min}(X)}$$

with $\sigma_{\max}(X)$ and $\sigma_{\min}(X)$ as the highest and lowest singular values of *X,* respectively. As a rule of thumb, $\kappa(X)$ requires attention if higher than 30[35].

The OLS fit was obtained with all the rs-fMRI variables and interpreted as the highest possible predictive power that could be extracted from the available features. However, it is well-known that, in the case of overparameterized linear models, OLS is generally not useful, as many CVs%, (i.e., percent error variance divided by the absolute value of the parameter estimates) are too high (CVs% > 100%) and the model is not *a posteriori* identifiable, so it should be rejected[37]. As discussed, performing feature selection at the individual level would lead to unstable estimates, so we continued to work at the group (i.e., NAD) level.

Eleven feature selection strategies, namely non-negative least squares (NNLS), elastic net regression, hierarchical clustering, stepwise selection, and general-to-specific modelling in different combinations were tested and compared to identify the best group of features to explain SUVR variability at group level. More details are in (**Supplementary Figure S4, Supplementary Table S1, Supplementary Methods**).

Full hierarchical modelling of the SUVR-fMRI relationship

As a NAD approach like the one described so far is statistically sound and unbiased only in case of low between-subject variability, a multilevel population modelling approach (mixed-effect model) was employed in order to characterize in a single stage both the group-level (fixed) and individual-level (random) effects[30] contributing to the relationship between the selected rs-fMRI variables and SUVR (**Figure 4***, top*). First, the link between model and SUVR was described at individual level by the following equation:

$$y_{Si} = F_{Si}(X_{Si}, \psi_{Si})$$

$$z_{Si} = y_{Si} + v_{Si}$$

with y_{Si} as the SUVR model prediction for the *i*th subject ($i = 1, \ldots, m$), which is a function of X_{Si} (the fixed-effects design matrix composed by the features extracted from the rs-fMRI data of

subject *i*), and the parameters to be estimated for subject *i*, ψ_{Si}; z_{Si} is the vector of the measured SUVR data of subject *i* and v_{Si} is the within-subject variability, or residual unexplained variability, assumed to be normally distributed with zero mean and variance σ_i^2.

Second, at population level, ψ_{Si} was described by a function combining population parameters (or fixed effects, θ_S), and random variability of individual parameters around the population mean (or random effects, η_{Si}), according to the following assumptions:

$$\eta_{Si} \sim N(0, \Omega_S)$$

$$\psi_{Si} = \theta_S + \eta_{Si}$$

where η_{Si} is assumed to be Gaussian, with zero mean, independent across individuals and with covariance matrix Ω_S (another population parameter); as a consequence, ψ_{Si} have a normal distribution as well. The matrix Ω_S was assumed to be full.

The intra-individual (first level) model structure was composed by the nine features selected with the NAD approach, here at single-subject level. Data normalization was performed within subjects via z-scoring. The inter-individual model (second level) describing the BSV of the parameters was set according to the aforementioned assumptions.

This estimation requires solving the penalized least squares problem, i.e., the penalized weighted residual sum of squares (PWRSS),

$$PWRSS(\Omega_S, \theta, y_{Si}|Z_{Si}) = WRSS(\Omega_S, \theta_S, y_{Si}|Z_{Si}) + \| y_{Si}|Z_{Si} \|^2$$

with Z_{Si} as the random-effects design matrix. This nonlinear optimization problem was solved using the restricted maximum likelihood (REML) estimation method[70]. The standard errors (SE) were calculated for each θ_S parameter estimate as the square root of the diagonal of their covariance matrix. The overall and subject-wise multilevel model R^2 were also evaluated. The residual unexplained variability v_{Si} was evaluated by calculating its median and variability (CV%) across subjects.

The hierarchical modelling approach was also performed across networks (*N*) in order to characterize between-network variability. RSNs were used as the grouping factor instead of subjects in a model formulated as follows:

$$y_{Nj} = F_{Nj}(X_{Nj}, \psi_{Nj})$$

$$z_{Nj} = y_{Nj} + v_{Nj}$$

with *j* as the *j*th network ($j = 1, \dots, q$). Normalization of SUVR and rs-fMRI variables was performed via z-scoring within RSNs.

The random effects η_{Nj} and the resulting individual parameters ψ_{Nj} were evaluated in terms of their correlation structure, both across RSNs (1st dimension) and across the nine predictors (2nd dimension), as seen in (**Figure 7b, c**).

Relative importance analysis to determine predictor importance

Relative importance analysis[40,71] was employed as a supplement to the results of hierarchical modelling. This type of analysis allows to appropriately partition the model's explained variance amongst multiple predictors when there is still significant multicollinearity, which makes typical indicators of importance (e.g., standardized regression coefficients) flawed. Dominance analysis (DA), in particular, works by rank-ordering the predictors in term of relative importance by comparing the additional contributions they make to the R^2 of all possible subset models. Specifically, we assessed the *general dominance* of the variables, which is established for one predictor over another when the average of its conditional contributions over all model sizes is greater than that of the other. The obtained general dominance weights are also measures of relative effect sizes, as they sum to the model R^2: the percent contribution to the model R^2 was therefore calculated and reported. While DA was originally proposed for OLS models, it was later extended to multilevel models[40]. In order to apply DA to hierarchical models, a null model with no predictors must be provided, and the slopes of first-level models must be considered fixed even when they are random in the identified model, to simplify dominance evaluation. DA was used to assess the extent to which each selected variable was driving the prediction in the context of the LME models across subjects (*S*) and across networks (*N*), as they were still affected by non-negligible multicollinearity.

Data availability

The multimodal [^{18}F]FDG PET and rs-fMRI data used in the present study can be accessed via request to the groups who performed the original studies[23,31]. Data sharing will be subject to the policies and procedures of the institution where each dataset was collected.

The codes and processed data that support the conclusions of this research work can be accessed via request to the corresponding authors.

Acknowledgements:

The authors would like to thank Dr. Valentin Riedl for making dataset A available, Dr. Chiara Favaretto for constructive suggestions for the analysis, and Dr. Mattia Veronese for his helpful and insightful observations on the final version of the manuscript.

Author contributions:

T.V. and A.B. designed the study, performed the analysis, interpretation of the data, and the drafting of the article. E.S. contributed to the preprocessing of the data and to the drafting of the article. M.C. contributed to the interpretation of the data and to the drafting of the article. M.A. designed and collected the data for the original study for dataset B and contributed to revision of the draft. All authors approved the final version of the article to be published.

Competing interests:

The authors declare no competing interests.

References

1. Sokoloff, L. *et al.* The [^{14}C]deoxyglucose method for the measurement of local cerebral glucose utilization: theory, procedure, and normal values in the conscious and anesthetized albino rat. *Journal of Neurochemistry* **28**, 897-916 (1977).
2. Bertoldo, A., Rizzo, G. & Veronese, M. Deriving physiological information from PET images: From SUV to compartmental modelling. *Clinical and Translational Imaging* **2**, 239–251 (2014).
3. Clarke, D. D. & Sokoloff, L. Circulation and energy metabolism in the brain. in *Basic Neurochemistry: Molecular, Cellular and Medical Aspects. 6th edition. Philadelphia: Lippincott-Raven* vol. 81 (1999).
4. Sokoloff, L. *et al.* The effect of mental arithmetic on cerebral circulation and metabolism. *Journal of Clinical Investigation* **34**, 1101–1108 (1955).
5. Raichle, M. E. The Brain's Dark Energy. *Science* **314**, 1249–1250 (2006).
6. Magistretti, P. J. & Allaman, I. A Cellular Perspective on Brain Energy Metabolism and Functional Imaging. *Neuron* **86**, 883–901 (2015).
7. Sokoloff, L. Energetics of Functional Activation in Neural Tissues. *Neurochemical Research* **24**, 321–329 (1999).
8. Biswal, B., Yetkin, F. Z., Haughton, V. M. & Hyde, J. S. Functional Connectivity in the Motor Cortex of Resting Human Brain Using Echo-Planar MRI. *Magnetic Resonance in Medicine* **34**, 537–541 (1995).
9. Fox, M. D. & Raichle, M. E. Spontaneous fluctuations in brain activity observed with functional magnetic resonance imaging. *Nat Rev Neurosci* **8**, 700–711 (2007).
10. Raichle, M. E. The restless brain: how intrinsic activity organizes brain function. *Phil. Trans. R. Soc. B* **370**, 20140172 (2015).
11. Cole, M. W., Bassett, D. S., Power, J. D., Braver, T. S. & Petersen, S. E. Intrinsic and task-evoked network architectures of the human brain. *Neuron* **83**, 238–251 (2014).

12. Thomas Yeo, B. T. *et al.* The organization of the human cerebral cortex estimated by intrinsic functional connectivity. *Journal of Neurophysiology* **106**, 1125–1165 (2011).
13. Allen, E. A. *et al.* Tracking whole-brain connectivity dynamics in the resting state. *Cerebral Cortex* **24**, 663–676 (2014).
14. Power, J. D. *et al.* Functional Network Organization of the Human Brain. *Neuron* **72**, 665–678 (2011).
15. van den Heuvel, M. P. & Sporns, O. Network hubs in the human brain. *Trends in Cognitive Sciences* **17**, 683–696 (2013).
16. Bullmore, E. & Sporns, O. The economy of brain network organization. *Nature Reviews Neuroscience* **13**, 336–349 (2012).
17. Shen, Q., Ren, H. & Duong, T. Q. CBF, BOLD, CBV, and CMRO2 fMRIrs-fMRI signal temporal dynamics at 500-msec resolution. *J. Magn. Reson. Imaging* **27**, 599–606 (2008).
18. Kim, S.-G. & Ogawa, S. Biophysical and Physiological Origins of Blood Oxygenation Level-Dependent fMRI Signals. *J Cereb Blood Flow Metab* **32**, 1188–1206 (2012).
19. Buxton, R. B. & Frank, L. R. A Model for the Coupling between Cerebral Blood Flow and Oxygen Metabolism during Neural Stimulation. *J Cereb Blood Flow Metab* **17**, 64–72 (1997).
20. Chen, J. E. *et al.* Resting-state "physiological networks". *NeuroImage* **213**, (2020).
21. Cecchin, D. *et al.* Brain PET and functional MRI: Why simultaneously using hybrid PET/MR systems? *Quarterly Journal of Nuclear Medicine and Molecular Imaging* **61**, 345–359 (2017).
22. Nugent, A. C., Martinez, A., D'Alfonso, A., Zarate, C. A. & Theodore, W. H. The Relationship between Glucose Metabolism, Resting-State fMRI BOLD Signal, and GABA A -Binding Potential: A Preliminary Study in Healthy Subjects and Those with Temporal Lobe Epilepsy. *J Cereb Blood Flow Metab* **35**, 583–591 (2015).
23. Aiello, M. *et al.* Relationship between simultaneously acquired resting-state regional cerebral glucose metabolism and functional MRI: A PET/MR hybrid scanner study. *NeuroImage* **113**, 111–121 (2015).

24. Marchitelli, R. *et al.* Simultaneous resting-state FDG-PET/fMRI in Alzheimer Disease: Relationship between glucose metabolism and intrinsic activity. *NeuroImage* **176**, 246–258 (2018).
25. Tomasi, D., Wang, G. J. & Volkow, N. D. Energetic cost of brain functional connectivity. *Proceedings of the National Academy of Sciences of the United States of America* **110**, 13642–13647 (2013).
26. Bernier, M., Croteau, E., Castellano, C. A., Cunnane, S. C. & Whittingstall, K. Spatial distribution of resting-state BOLD regional homogeneity as a predictor of brain glucose uptake: A study in healthy aging. *NeuroImage* **150**, 14–22 (2017).
27. Wang, J. *et al.* The Relationship Among Glucose Metabolism, Cerebral Blood Flow, and Functional Activity: a Hybrid PET/fMRI Study. *Mol Neurobiol* (2021).
28. Shokri-Kojori, E. *et al.* Correspondence between cerebral glucose metabolism and BOLD reveals relative power and cost in human brain. *Nat Commun* **10**, 690 (2019).
29. Cabral, J. *et al.* Cognitive performance in healthy older adults relates to spontaneous switching between states of functional connectivity during rest. *Scientific Reports* **7**, (2017).
30. Hox, J. J., Moerbeek, M. & Schoot, R. van de. *Multilevel analysis: techniques and applications*. Routledge (2017).
31. Riedl, V. *et al.* Local Activity Determines Functional Connectivity in the Resting Human Brain: A Simultaneous FDG-PET/fMRI Study. *Journal of Neuroscience* **34**, 6260–6266 (2014).
32. Schaefer, A. *et al.* Local-Global Parcellation of the Human Cerebral Cortex from Intrinsic Functional Connectivity MRI. *Cerebral Cortex* **28**, 3095–3114 (2018).
33. Wang, H. & Yushkevich, P. A. Multi-atlas segmentation with joint label fusion and corrective learning—an open source implementation. *Front. Neuroinform.* **7**, (2013).
34. Wu, G.-R. *et al.* A blind deconvolution approach to recover effective connectivity brain networks from resting state fMRI data. *Medical Image Analysis* **17**, 365–374 (2013).

35. Belsley, D. A. *Conditioning diagnostics: collinearity and weak data in regression*. (Wiley, 1991).
36. Benjamini, Y. & Hochberg, Y. Controlling the False Discovery Rate: A Practical and Powerful Approach to Multiple Testing. *Journal of the Royal Statistical Society: Series B (Methodological)* **57**, 289–300 (1995).
37. Cobelli, C., Foster, D. & Toffolo, G. Identifiability of the tracer model. in *Tracer Kinetics in Biomedical Research* 109–163.
38. Meinshausen, N. Sign-constrained least squares estimation for high-dimensional regression. *Electronic Journal of Statistics* **7**, 1607–1631 (2013).
39. Zou, H. & Hastie, T. Regularization and variable selection via the elastic net. *J Royal Statistical Soc B* **67**, 301–320 (2005).
40. Luo, W. & Azen, R. Determining Predictor Importance in Hierarchical Linear Models Using Dominance Analysis. *Journal of Educational and Behavioral Statistics* **38**, 3–31 (2013).
41. Liang, X., Zou, Q., He, Y. & Yang, Y. Coupling of functional connectivity and regional cerebral blood flow reveals a physiological basis for network hubs of the human brain. *Proceedings of the National Academy of Sciences* **110**, 1929–1934 (2013).
42. Honey, C. J. *et al.* Predicting human resting-state functional connectivity from structural connectivity. *PNAS* **106**, 2035–2040 (2009).
43. Bi, Q. *et al.* Relationship between the disrupted topological efficiency of the structural brain connectome and glucose hypometabolism in normal aging. *NeuroImage* **226**, (2021).
44. Chen, Y., Lin, Q., Liao, X., Zhou, C. & He, Y. Association of aerobic glycolysis with the structural connectome reveals a benefit–risk balancing mechanism in the human brain. *Proc Natl Acad Sci USA* **118**, e2013232118 (2021).
45. Thompson, W. H. & Fransson, P. The mean–variance relationship reveals two possible strategies for dynamic brain connectivity analysis in fMRI. *Front. Hum. Neurosci.* **9**, (2015).

954 46. Hellyer, P. J. *et al.* Protein synthesis is associated with high-speed dynamics and broad-band
955 stability of functional hubs in the brain. *NeuroImage* **155**, 209–216 (2017).
956 47. Deng, L., Sun, J., Cheng, L. & Tong, S. Characterizing dynamic local functional connectivity
957 in the human brain. *Scientific Reports* **6**, (2016).
958 48. Zhang, X., Pan, W.-J. & Keilholz, S. D. The relationship between BOLD and neural activity
959 arises from temporally sparse events. *NeuroImage* **207**, 116390 (2020).
960 49. Howarth, C., Mishra, A. & Hall, C. N. More than just summed neuronal activity: how multiple
961 cell types shape the BOLD response. *Phil. Trans. R. Soc. B* **376**, 20190630 (2021).
962 50. Henriksen, O. M. *et al.* Interindividual and regional relationship between cerebral blood flow
963 and glucose metabolism in the resting brain. *J Appl Physiol (1985)* **125**, 1080–1089 (2018).
964 51. Muthukumaraswamy, S. D., Evans, C. J., Edden, R. A. E., Wise, R. G. & Singh, K. D.
965 Individual variability in the shape and amplitude of the BOLD-HRF correlates with
966 endogenous GABAergic inhibition. *Hum. Brain Mapp.* **33**, 455–465 (2012).
967 52. Li, Z., Zhu, Y., Childress, A. R., Detre, J. A. & Wang, Z. Relations between BOLD fMRI-
968 Derived Resting Brain Activity and Cerebral Blood Flow. *PLoS ONE* **7**, e44556 (2012).
969 53. Tong, Y. *et al.* Perfusion information extracted from resting state functional magnetic
970 resonance imaging. *J Cereb Blood Flow Metab* **37**, 564–576 (2017).
971 54. Huisman, M. C. *et al.* Cerebral blood flow and glucose metabolism in healthy volunteers
972 measured using a high-resolution PET scanner. *EJNMMI Res* **2**, 63 (2012).
973 55. Fan, A. P., Jahanian, H., Holdsworth, S. J. & Zaharchuk, G. Comparison of cerebral blood
974 flow measurement with [15 O]-water positron emission tomography and arterial spin labeling
975 magnetic resonance imaging: A systematic review. *Journal of Cerebral Blood Flow and*
976 *Metabolism* **36**, 842–861 (2015).
977 56. Fan, A. P. *et al.* Quantification of brain oxygen extraction and metabolism with [15O]-gas
978 PET: A technical review in the era of PET/MRI. *NeuroImage* **220**, (2020).

57. Kundu, P. *et al.* Multi-echo fMRI: A review of applications in fMRI denoising and analysis of BOLD signals. *NeuroImage* **154**, 59–80 (2017).
58. Hamberg, L. M. *et al.* The dose uptake ratio as an index of glucose metabolism: useful parameter or oversimplification? *J Nucl Med* **35**, 1308–1312 (1994).
59. Peretti, D. E. *et al.* Relative cerebral flow from dynamic PIB scans as an alternative for FDG scans in Alzheimer's disease PET studies. *PLoS ONE* **14**, e0211000 (2019).
60. Glasser, M. F. *et al.* The Human Connectome Project's neuroimaging approach. *Nat Neurosci* **19**, 1175–1187 (2016).
61. Tustison, N. J. *et al.* N4ITK: Improved N3 Bias Correction. *IEEE Trans. Med. Imaging* **29**, 1310–1320 (2010).
62. Fischl, B., Sereno, M. I. & Dale, A. M. *Cortical Surface-Based Analysis II: Inflation, Flattening, and a Surface-Based Coordinate System*. http://www.idealibrary.com (1999).
63. Jenkinson, M., Beckmann, C. F., Behrens, T. E. J., Woolrich, M. W. & Smith, S. M. FSL. *NeuroImage* **62**, 782–790 (2012).
64. Byrnes, K. R. *et al.* FDG-PET imaging in mild traumatic brain injury: A critical review. *Frontiers in Neuroenergetics* **6**, (2014).
65. Avants, B. B. *et al.* A reproducible evaluation of ANTs similarity metric performance in brain image registration. *NeuroImage* **54**, 2033–2044 (2011).
66. Behzadi, Y., Restom, K., Liau, J. & Liu, T. T. A component based noise correction method (CompCor) for BOLD and perfusion based fMRI. *NeuroImage* **37**, 90–101 (2007).
67. Ciric, R. *et al.* Benchmarking of participant-level confound regression strategies for the control of motion artifact in studies of functional connectivity. *NeuroImage* **154**, 174–187 (2017).
68. Marcus, D. S. *et al.* Informatics and Data Mining Tools and Strategies for the Human Connectome Project. *Front. Neuroinform.* **5**, (2011).

69. Chen, J. E. & Glover, G. H. BOLD fractional contribution to resting-state functional connectivity above 0.1 Hz. *NeuroImage* **107**, 207–218 (2015).

70. Laird, N. M. & Ware, J. H. Random-effects models for longitudinal data. *Biometrics* **38**, 963–974 (1982).

71. Tonidandel, S. & LeBreton, J. M. Relative Importance Analysis: A Useful Supplement to Regression Analysis. *J Bus Psychol* **26**, 1–9 (2011).

Supplementary Files

This is a list of supplementary files associated with this preprint. Click to download.

- ManuscriptVolpietalNatCommunSupplementary.docx